

Deliverable

Deliverable 2.2 - Comparison of different techniques for induced seismicity monitoring

Report information	
Work package	WP2 Innovation in real-time monitoring and big-data analysis for EGS
Lead	ETH, IEG
Authors	Claudia Finger, Peidong Shi, Katinka Tuinstra, Federica Lanza, Juan Porras & Francesco Grigoli
Reviewers	[Luigi Passarelli]
Approval	Stefan Wiemer
Status	Draft
Dissemination level	Internal
Will the data supporting this document be made open access?	Yes
If No Open Access, provide reasons	-
Delivery deadline	31.05.2022
Submission date	22.06.2022
Intranet path	[DOCUMENTS/DELIVERABLES/Deliverable2.2.docx]



Table of Contents

Summary 3

1. Introduction 3

2. Data sets 4

2.1. COSEISMIQ..... 4

2.2. GeMEX 4

2.3. FORGE 2019 Pilot Stimulation 4

2.3.1. Hazard and reservoir monitoring networks..... 5

2.4. Preliminary synthetic data set for FORGE 6

3. Detection of microseismic events and arrival times of seismic phases..... 6

3.1. A microseismic event detector for DAS data 6

3.1.1. Application to the FORGE 2019 stimulation dataset 7

3.2. A new picking algorithm for DAS data..... 8

3.3. Machine-Learning based picker algorithms..... 9

3.3.1. Application to the FORGE 2019 stimulation dataset 10

3.4. Conventional automatic picker algorithms..... 11

3.4.1. Application to the FORGE 2019 stimulation dataset 11

4. Location of single and clustered microseismic events 12

4.1. Relative Cluster Location algorithm for DAS data..... 12

4.1.1. Application to the FORGE 2019 stimulation dataset (natural seismicity)..... 14

4.2. Backprojection of phase probabilities..... 15

4.2.1. Application to the COSEISMIQ, Iceland, dataset 16

4.3. Earthquake locations from elastic Time-Reverse Imaging (TRI) 17

4.3.1. Application to Los Humeros, Mexico, dataset 17

4.3.2. Application to preliminary synthetic dataset at the FORGE EGS site 19

5. Conclusions and Outlook..... 20

Reference List..... 23

Summary

In this deliverable we report on a suite of both conventional and newly developed methods and workflows for the detection and location of induced (micro-) seismicity in geothermal reservoirs. We discuss the necessary resources (e.g., HPC, type of velocity information, GPU), recording equipment (e.g., number of stations, type of sensors used), typical accuracies (e.g., spatial uncertainties, temporal precision), computational cost (per second of data or per event), and level of automatization. We explore conventional approaches, as well as machine learning and waveform-based workflows. The goal is to give a comprehensive overview from which to identify the optimal methods on the basis of available resources, achieved accuracy, real-time capabilities, and/or processing time from data gathering to final results.

This deliverable constitutes a first report on the current work, and in the future, we will systematically compare the presented algorithms using a common synthetic dataset. This dataset is under development and will be the foundation for a standardized benchmark aimed at a rigorous comparison of (micro-) seismic monitoring approaches in terms of computing performances and accuracies of detections and locations.

1. Introduction

In recent years, the number of sensors deployed at geothermal project sites has increased exponentially. As a consequence, we have seen an increase in recorded seismic data volume along with a reduction in location uncertainties and magnitude of completeness. These very large datasets thus offer a very high potential for investigating (micro-) seismicity in geothermal reservoirs with an unprecedented level of detail. However, for these investigations to be useful during geothermal operations, results need to be available in near real time and with low uncertainties. Only then can forecasting procedures and modern reaction protocols, such as Adaptive Traffic Light Protocols (ATLP), take their full effect in ensuring safe operations.

In this deliverable, we present and compare (1) a newly developed semblance-based method for fast detection of microseismicity in DAS record streams (section 3.1), (2) three picking algorithms, including a cross-correlation based picker for DAS (section 3.2), a new machine learning based phase probability picker and location workflow (MALMI, Shi et al., 2022; see also D2.1, sections 3.3, 4.2), and the well-established nonparametric autopicker method of Rawles & Thurber (2015), *kpick* (section 3.4); and (3) two types of location algorithms: HADES, a clustered event relocation algorithm based on a distance geometry problem (Grigoli et al., 2021; section 4.1) and time-reverse imaging or backprojection location schemes (section 4.2, 4.3, Li et al., 2020).

Here, we show the initial results of each approach on available datasets, namely the 2019 FORGE stimulation data, the COSEISMIQ dataset collected in Iceland (Grigoli et al., 2022) and the GeMEX dataset collected in Los Humeros, Mexico (Toledo et al., 2020). We also show results from preliminary synthetic waveform data that mimic the geological situation at the FORGE site. When possible (e.g., the same dataset is used) we make a qualitative comparison of the results in terms of accuracy, computational efficiency, and assumptions. We then conclude with some outlook for future development.

2. Data sets

2.1. COSEISMIQ

The project COSEISMIQ (Control SEISmicity and Manage Induced earthQuakes, <http://www.coseismiq.ethz.ch/en/home/>), also funded by GEOTHERMICA, was a predecessor of the current DEEP project as it also aimed at integrating innovative seismic monitoring and imaging techniques, geomechanical models and risk analysis method with the ultimate objective to develop safe and sustainable geothermal energy systems. In COSEISMIQ, the active geothermal system in the Hengill region in Iceland was chosen as a well-rounded demonstration site. This region is located in the southern end of the Western Volcanic Zone (WVZ), at the triple junction between the WVZ, the Reykjanes Peninsula (RP), the landward extension of the Reykjanes spreading ridge, and the South Iceland Seismic Zone (SISZ). Due to its complex tectonic setting and the ongoing geothermal operations in the area, several thousand natural and induced seismic events occur every year. In the Hengill area, the permanent seismic network is run by the Iceland GeoSurvey (ISOR) and the Icelandic Meteorological Office (IMO) and comprises a total of 14 stations. In November 2018, within the framework of the project COSEISMIQ, the network was densified with 26 additional temporary stations. This temporal network includes 9 broadband STS-2 (120s), 5 Guralp 6D (30s) and 12 short-period 5s-Lennartz. During the monitoring period from 2 November 2018 to 2 July 2020, ISOR reported a total of 12,157 events in the Hengill region, 69 of them with magnitudes larger than M_L 2.0 (Grigoli et al., 2022). Seismic sequences in this area are usually characterized by spatial and temporal clustering and small magnitudes below the resolution of regional networks. This makes the COSEISMIQ dataset a perfect application for testing new seismic data analysis workflows as we aim at pushing detectability and location of smaller magnitude events, which we expect to be produced in deep geothermal stimulations. In section 4.2, we process one month of continuous seismic data from 41 stations of the augmented Hengill network and compare with existing seismic catalogs related to the microseismic monitoring operations carried out for the project COSEISMIQ.

2.2. GeMEX

The project GeMEX (Cooperation in Geothermal energy research Europe-Mexico for development of hot enhanced (hot-EGS) and super-hot geothermal systems (SHGS), funded by Horizon 2020, aimed at advancing the development and exploitation strategies for unconventional geothermal resources. One of two chosen sites for the project is the geothermal field of Los Humeros, Mexico, which is an actively producing geothermal field with numerous injection and production wells. The northern part of the area is much hotter ($>380^{\circ}\text{C}$) than the wells used for production today. The development of this part of the reservoir presents a challenge, both because of the high temperature and because of the water chemistry. In addition, the area was only poorly characterized by geophysical and geological surveys before the project. Extensive passive seismic monitoring was carried out between September 2017 and September 2018 with a total of 27 three-component seismic stations (Toledo et al., 2019). 25 broadband stations (22 Trillium C-120s and 3 Trillium C-20 PH) recording at 200 Hz, and 20 short period stations (Mark L-4C-3D) recording at 100 Hz are deployed at the surface with an average inter-station distance of 1.6 km to 2 km and a total aperture of 30 km. A preliminary catalog was provided by Gaucher et al. (2019). To test the application and accuracy of TRI in a less-than optimal setting, this dataset, with its inadequate station distribution for TRI (Finger & Saenger, 2020) and only a one-dimensional velocity model (Löer et al., 2020) is the perfect candidate.

2.3. FORGE 2019 Pilot Stimulation

The U.S. Department of Energy FORGE is a dedicated international underground field laboratory in Utah and the selected demonstration test site within the DEEP project. Its purpose is to develop, test, and accelerate breakthroughs in EGS. FORGE is located in a low-risk area in the vicinity of the town of Milford in Beaver County, Utah, on the western flank of the Mineral Mountains (Moore et al., 2019; Wannamaker et al., 2020; Pankow et al., 2020). The site is in continuing development with new wells and instrumentation being drilled/added. In this deliverable, we used the wells and network configuration in place at the time of the 2019 stimulation, as data from the current monitoring network, which was used in the most recent April 2022 stimulation, is currently not available as it is being pre-processed at the time of writing.

2.3.1. Hazard and reservoir monitoring networks

In 2019, in addition to stations of the Utah Regional Seismic Network (URSN), surface monitoring consisted of five surface broadband stations, three accelerometers, of which one was placed in a shallow well (68-32), and several temporary high-density (nodal) experiments in various configurations covering the footprint of the FORGE site. Among the wells drilled at FORGE, well 58-32 was used for stimulation and well 78-32, located about 400 m east-southeast of 58-32, was used for deep seismic monitoring (Figure 1). Well 78-32 was equipped with an industry-grade 12-level geophone string deployed by Schlumberger, and an optical fiber in a metal tube, cemented behind the casing. The geophones were positioned at depths of 645-980 m, with 30.5 m spacing between each sensor. They were only recording during the stimulation. The installed fiber was engineered by Silixa and interrogated using the Carina system (Naldrett et al., 2020). Distributed Acoustic Sensing (DAS) data was acquired with a 1 m channel spacing using a 10 m gauge length. An example of the DAS data in the well 78-32 from the 2019 pilot stimulation is given in Figure 2, featuring both a microseismic event from the stimulation, as well as a recorded earthquake from a cluster approximately 3 km to the east of the borehole. Note the high spatial coherence measured by the DAS of the wavefield.

Both geophone data and DAS data are openly available for download at the Geothermal Data Repository (GDR) website (<https://gdr.openei.org/forge>). Data from the temporary 151 nodal surface stations is available through the University of Utah website (<https://constantine.seis.utah.edu/index.html>). Near the FORGE project's completion all the waveform data collected will be transferred to the Incorporated Research Institutions for Seismology Data Management Center (IRIS DMC).

For testing our new picking and location methods (sections 3 and 4) for both velocity and strain-rate (DAS) data, here we focus on the microseismic catalog of ca. 400 events constructed from the downhole geophones by Schlumberger. The Schlumberger catalog thus constitutes our initial reference ground truth. We note here, however, that, due to proprietary information issues, we do not know the full details of the different steps taken during the processing of the data, and thus use the downhole catalog as supplied by the contractor. In addition, for the DAS data, as a fundamental step for testing the theory and capability of the methods, we also simulated synthetic data based on the 2019 FORGE network configuration.

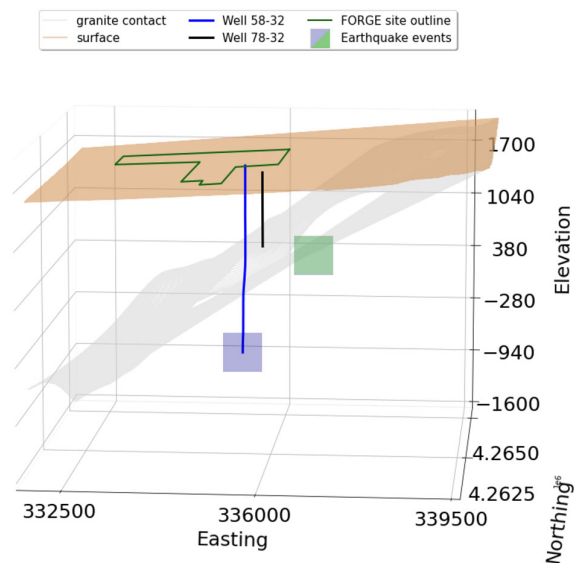


Figure 1. Utah FORGE network configuration for the 2019 pilot stimulation. The FORGE footprint is in green; the pilot stimulation well 58-32 is indicated by a blue line; whereas the monitoring well 78-32 is shown in black. Blue square - stimulation zone, green square - natural earthquakes zone. The domain contains a strongly dipping granitic layer, everything below the gray surface is the granitic layer, and everything above is a sedimentary basin. Depth is depicted as meter .a.s.l.

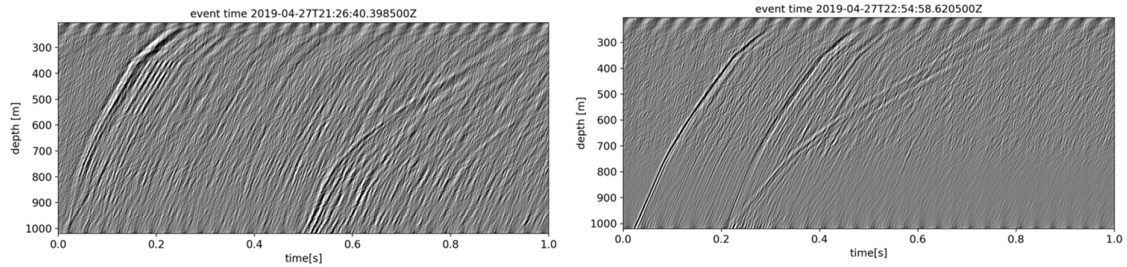


Figure 2. Two events recorded by the DAS cable, zero-time taken 0.075 before the event detection time, processed using an F-K filter, trace muting and global normalization. The left image shows one of the microseismic events originating from the 2019 stimulation zone. It shows a clear P-wave arrival at the bottom of the cable just after the zero-time, and an S-wave arrival as well as a second P-wave arrival at 0.25, that is probably caused by interaction of the wavefield with the granitic layer that is roughly located at the bottom of the cable. The right image shows a regional earthquake that originated in a cluster about 3 km to the east of the borehole. Here there is also a clear P-wave arrival just after 0s, and an S-wave arrival at 0.5 s. The larger lag time between the P- and S-wave shows that this event took place further away.

2.4. Preliminary synthetic data set for FORGE

To compare the performance of different seismic monitoring algorithms, we need to adopt a standardized testbench approach. As a starting point, we are building a wave propagation modeling workbench in order to conveniently and systematically define simulations of microearthquakes and test detection and location methods. A synthetic testbench has the prevailing advantage that the ground truth (i.e., the true number of sources, their origin time and their location) is known. For each method, locations with uncertainties can be directly compared to the ground truth and an absolute error can be reported. For the synthetic testbench, we aim at creating a digital twin of the FORGE EGS site in Utah, USA. To this end, the elastic full wavefield is simulated using a three-dimensional model of shear-wave velocity (V_s) and compressional-wave velocity (V_p) derived for the FORGE footprint derived from previous studies (Lellouch et al., 2020; Zhang & Pankow, 2021). We then use synthetic source locations from both the earthquake catalogs compiled during the 2019 pilot stimulation at FORGE and the one obtained during the recent stimulation in April 2022 to ensure realistic magnitude-frequency relations and realistic source distributions. Coherent and incoherent noise will be added to the simulations for maximum complexity. Receivers can be placed at arbitrary locations in the model domain and can be used to test different sensor distributions and network configurations (i.e., inter-sensor spacings, surface vs. borehole sensors, azimuthal coverage). Displacement as well as strain data will be recorded to investigate different sensor types (traditional seismometers and distributed acoustic sensing systems (DAS)). The synthetic testbench is currently in development and will be used to update the information performances of the methods presented in this initial report.

3. Detection of microseismic events and arrival times of seismic phases

In the following sections we describe new and modified methods for the detection and the identification of phase arrival times of microseismicity.

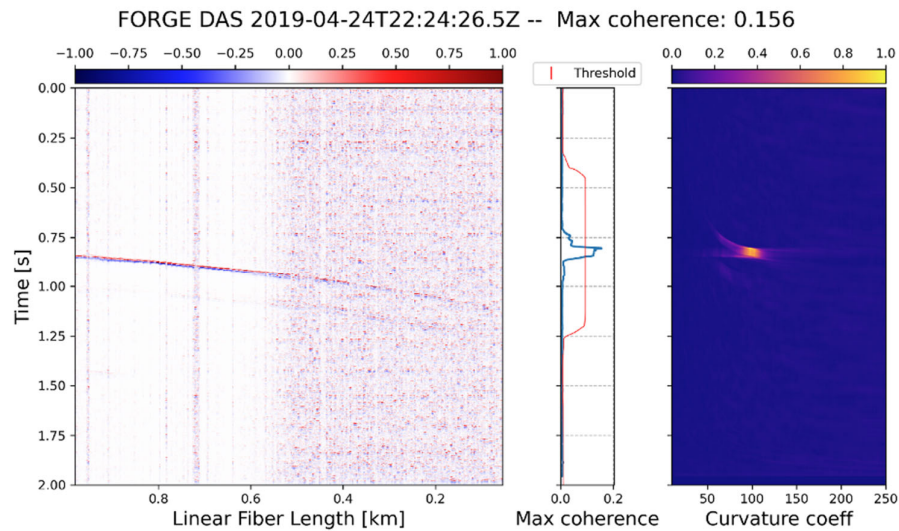
3.1. A microseismic event detector for DAS data

DAS systems collect data in the order of 10^3 - 10^2 Terabytes per experiment (Quinteros et al., 2021). This leads to limitations in regards to the capacity of permanent waveform archival and therefore, a possible solution is to store only the data containing the events. To do so, new algorithms for real-time detection must be established, since the standard approaches fail as they are either computationally expensive or do not fully exploit the high spatial density of DAS arrays. Here we present a semblance-based near real-time microseismic event detector that fully exploits the DAS high spatial sampling and allows to measure the coherency of the seismic wavefield.

As DAS data are inherently noisier than conventional geophones, any event detection algorithm applied to DAS should include pre-processing steps (e.g., linear and median filtering, frequency-wavenumber filter) aimed at denoising the raw data. The event detector proposed here is based on a modified version of the semblance function (Neidell & Taner, 1971) that makes use of the data itself as the only input. The detector identifies seismic events by looking at waveform coherence along geometrical hyperbolas while changing the curvature and position of the vertex, thus leaving aside the dependency on physical parameters such as velocity. The method returns a time series of coherence values and, if these values are higher than a determined threshold, a seismic event is detected. This approach fully exploits the high spatial density of the seismic wavefield recorded with DAS without any data conversion and no other input than the data itself, reducing the computational time otherwise required by conventional detection methods. Several tests demonstrated that the best performances of the algorithm are obtained when the derivative of the STA/LTA stacking function is used as input data (for more details on the method, see deliverable D2.3).

3.1.1. Application to the FORGE 2019 stimulation dataset

We applied the detector to a test sample of 110 events recorded by the DAS cable installed at FORGE site (well 78-32) during the 2019 stimulation. Discrimination of real versus false events is based on a dynamic threshold function, defined as the mean of the coherency vector plus 2.5 standard deviations in a time window defined as the 40% of the total duration of the input data. Moreover, after the declaration of a real event, we halted the discrimination function for 1 second to make sure S-waves arrivals do not trigger a separate event. The computing time (serial code) is approximately 4 seconds per each second of data measured in a laptop with an Intel quad-core i7 processor and 16 GB of Random Access Memory (RAM). These numbers are based on downsampled data and indicate that real-time is currently not possible, but it is promising with the adequate optimization. Figures 3a, b, and c, show the results of the detection algorithm for three example events. The first event (Figure 3a) is a perforation shot, displaying high amplitude with a clear wavefield and maximum in the coherency panel. The second event (Figure 3b) is a weak (low SNR) microseismic event, but it is still well detected by the algorithm. The last event is extremely noisy (Figure 3c), and the algorithm is not able to detect any maximum and it is therefore classified as false detection. Overall, the rate of detected events is equal to 72% (79 events of the 110 events considered as the ground truth). A visual inspection of the missing 31 events shows that the events are indeed not visible in time nor in frequency domains in the DAS data, and can be slightly identified in the geophone array, which has higher sensitivity than DAS. Therefore, those events are below the SNR of the denoised DAS data and not detectable by the algorithm. We conclude that this new semblance-based DAS detector is able to correctly identify all the events that are effectively visible in the data.



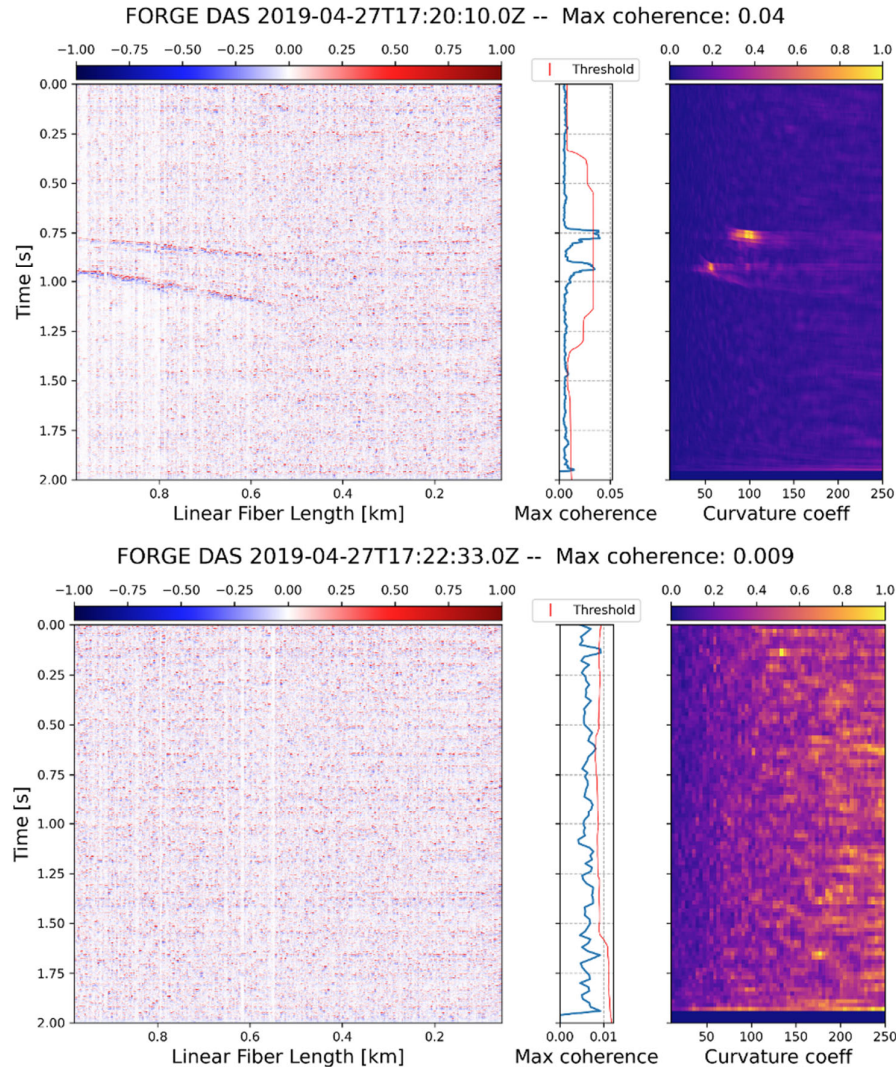


Figure 3. Example of the semblance-based detector performances on three test events of different signal-to-noise ratio: a) Perforation shot, characterized by a well-defined P-wave arrival at ~ 0.8 s. On the right, the coherence panel shows a well-defined maximum in correspondence of the event. b) Microseismic event, with the P-wave arrival at ~ 0.76 s and the S-wave at ~ 0.9 s. On the right, the coherence panel shows a well-defined maximum in correspondence of P and S phases, c) Noise, the coherency panel that does not show any well-defined maxima. At ~ 0.2 s the coherency vector overcomes the threshold but it is classified as a false detection.

3.2. A new picking algorithm for DAS data

Once an event is detected, many location algorithms require picks of the P- and S-wave arrival times. Although picking for conventional seismic (velocity) data is a mature field with numerous software readily available, these techniques, similarly to the classical methodologies for earthquake detection, often fail or prove inefficient when used with the large amount of data and low signal-to-noise quality recorded by DAS. Here we describe a new picking algorithm for DAS. Both microseismicity and natural earthquake data collected during the FORGE 2019 pilot stimulation (blue and green squares in Fig. 1) were used for testing/training.

Classical picking methods face many challenges when applied to DAS data. For example, STA/LTA pickers cannot be uniquely tuned to accommodate the largely different magnitudes and signal-to-noise ratios found in the data. Likewise, more sophisticated pickers such as e.g., Phasenet (Zhu & Beroza, 2019) often require three components and expensive computational power, which are not always available. Thus, we have developed a semi-automatic method based on user-defined hand-picks, interpolation and cross-correlations. The full workflow is shown in Figure 4. The DAS data is preprocessed in python by trace muting, global normalization, bandpass filtering between 5-250 Hz, an FK filter to

remove the zero-wavenumber noise and a 2D-median filter. Consecutively, via a MATLAB interactive GUI, the user clicks a predefined number of hand-picks (pluses in Figure 4a) around the P-wave and S-wave arrival times. Linear interpolation along these hand-picks is performed and extrapolated around an adjustable time interval following the hand-picks (blue and red lines in Fig. 4a), that is set slightly longer for the S-wave picks to accommodate for its longer waveform. If the user defines fewer hand-picks the interpolation could be set to spline interpolation to accommodate for the curvature of the wavefield between fewer points. The hand-picks are then stacked to form a wavelet template of a defined time-width (Fig. 4b). Subsequently, this stacked wavelet is cross-correlated with all traces along the DAS cable, within the given time intervals. This process is done separately for the P- and S-phase arrivals. The final picks for all traces correspond to the maximum cross correlation values (Fig. 4c).

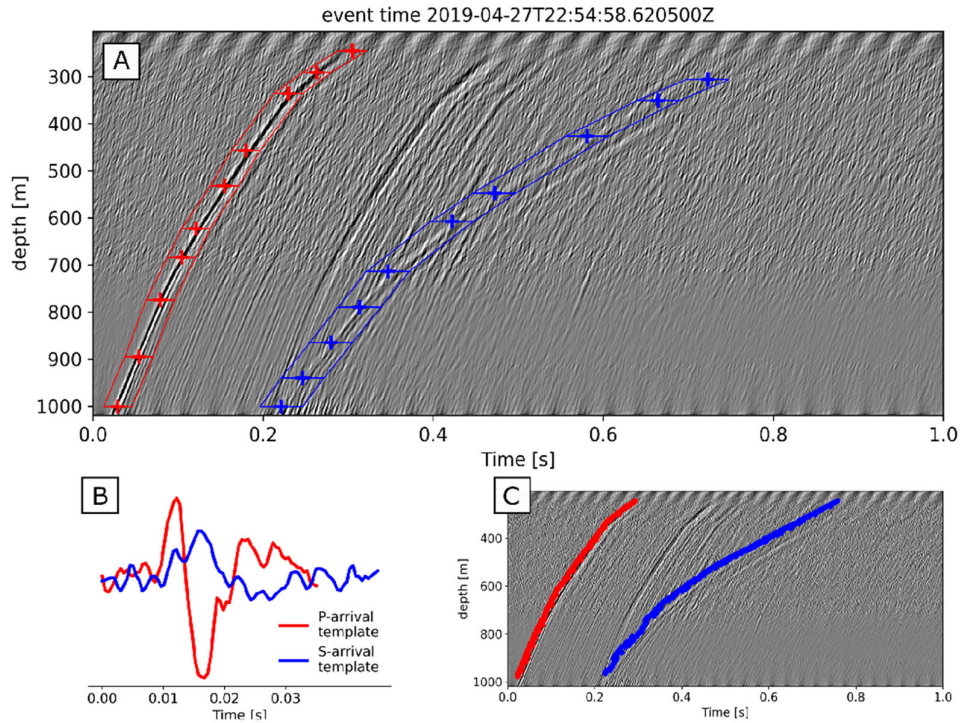


Figure 4. Workflow of the MATLAB-based picking algorithm for DAS data. a) hand picks of P-wave and S-wave arrival times; b) wavelet template derived from stacked handpicks over a pre-defined time window, c) final picks for all traces.

3.3. Machine-Learning based picker algorithms

Machine Learning (ML) based methods provide a promising way of analyzing large datasets in an automated way. Previous studies have shown that ML-based picking methods can achieve comparable or even superior picking accuracy to manual picks and, at the same time, operate with very high efficiency, not inferior to classical automatic picking algorithms such as STA/LTA (Zhu & Beroza, 2019; Mousavi et al., 2020). In this section, we demonstrate the application of ML-based phase pickers on an induced microseismic dataset with a very high sampling rate (2000 Hz). The obtained pickers or phase probabilities from ML models can be further used in a classical traveltime-based location algorithm or a waveform-based location algorithm to locate events in a fully automatized workflow (section 4.2).

Pre-trained Machine Learning (ML) models (Ross et al., 2018; Zhu & Beroza, 2019; Mousavi et al., 2020, Woollam et al., 2022) enable us to directly apply existing ML models to a new dataset to generate phase picks or continuous phase probabilities from raw seismic waveforms. This is especially beneficial in conjunction with continuous waveform-based location methods such as in MALMI (MACHINE Learning aided earthquake MLgration location; see Deliverable 2.1; Shi et al., 2022, and section 4.2). Currently, most ML models for phase picking are trained on local, regional or global earthquake datasets whereas microseismic events with magnitude smaller than 0 are extremely under-represented and seismic data are recorded at a sampling rate ranging from 50-200 Hz. Therefore, we need to examine the performance of pre-trained models on the induced earthquake dataset where low magnitude microseismic events are dominant and/or high sampling rate data are acquired.

3.3.1. Application to the FORGE 2019 stimulation dataset

We test the ML phase picking performance on the FORGE 2019 pilot stimulation dataset (blue square in Fig. 1). This microseismic dataset was collected at the Utah FORGE geothermal site at a sampling rate of 2000 Hz by 12-level geophones deployed in a vertical borehole (well 78-32) during the injection of high-pressure fluids. We evaluated different ML models and data pre-processing strategies to feed to ML models (Figures 5, 6 and 7). We identified the best-fit ML model through the quantitative comparisons among the different ML models (including Generalize Phase Detection - GDP, PhaseNet and EQ-Transformer). To gain better prediction performance of ML models on the small scale microseismic events, we tested the pre-processing strategy of modifying the sampling rate of the seismic meta-data to enlarge the scale of the microseismicity to a similar scale of local or regional earthquakes and feeding the modified data to the pre-trained ML models. We note that the EQ-Transformer model works well on the re-scaled traces with multiple events, events with short inter-event times, and exhibits comparable picking precision with manual picks (Figure 8). We conclude that microseismic events with low magnitude (below M_L -0.5 or -1) have distinct waveform features than the local and regional earthquakes of larger magnitude (>0), thus cannot be predicted well by all the pre-trained ML models tested using original data. However, re-scaling the microseismic events is an efficient way to increase the ML model performance on seismic events of different magnitudes (Figures, 5, 6, and 7).

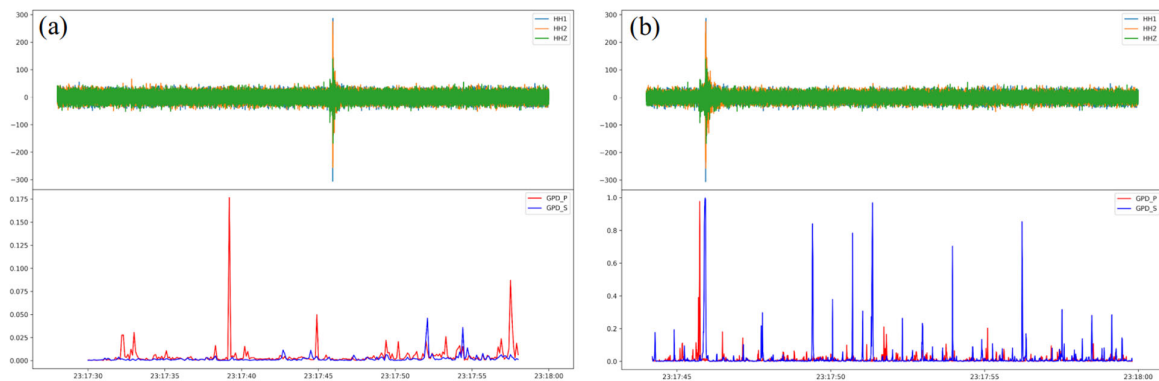


Figure 5. Event identification and phase picking results of the GPD (Generalize Phase Detection) ML model (Ross et al., 2018) on (a) the original data and (b) the re-scaled data.

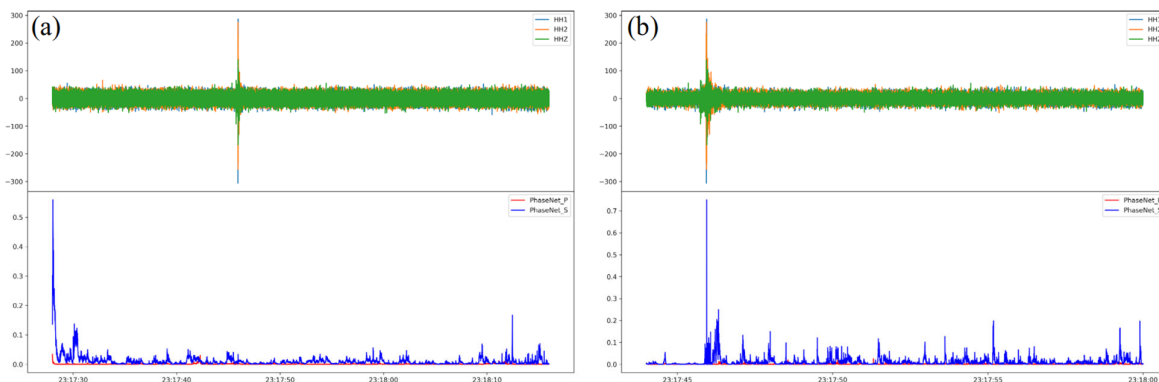


Figure 6. Event identification and phase picking results of the PhaseNet ML model (Zhu et al., 2019) on (a) the original data and (b) the re-scaled data.

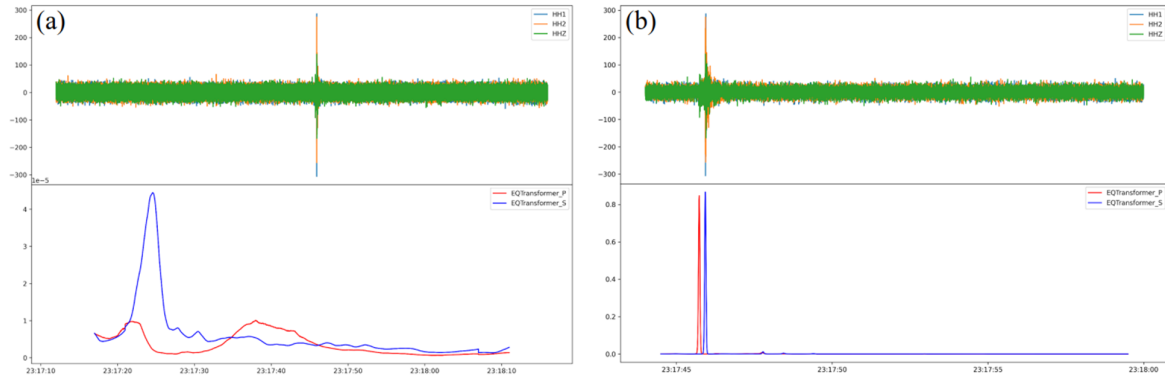


Figure 7. Event identification and phase picking results of the EQ-Transformer ML model (Mousavi et al., 2020) on (a) the original data and (b) the re-scaled data.

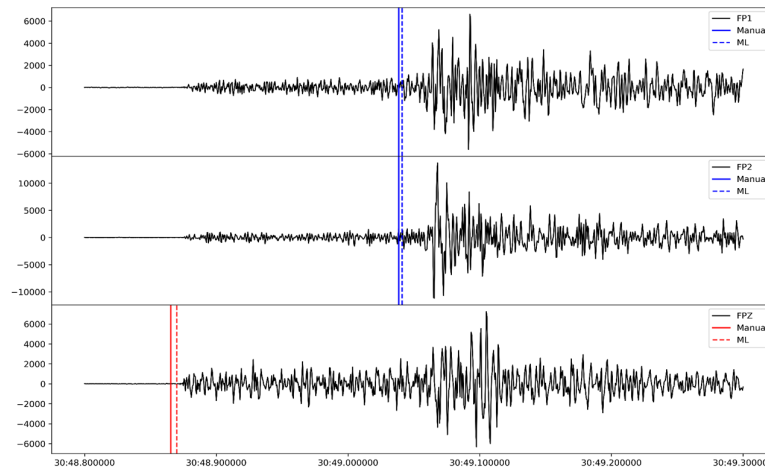


Figure 8. Comparison between the manual picks (solid line) and the ML picks of the best-fit model (dashed line) for P- and S-phases of a Mw -0.7 microseismic event.

3.4. Conventional automatic picker algorithms

Accurate identification of phase arrival times is essential to assure high-precision earthquake locations in standard workflows. In order to compare the performance of conventional picking methods with emerging waveform-based and machine-learning based methods, we have chosen the non-parametric autopicker method of Rawles & Thurber (2015), *kpick*. This algorithm is user-friendly, fast, data-driven and robust for automatically detecting P- and S-wave arrivals based on a nearest neighbors-based approach. The strength of this algorithm resides in the fact that the method uses the data itself to define the model, rather than building a model by estimating parameters from the data. *kpick* produces a score function defined as the ratio of the similarity of a given trace to a set of ‘positive’ reference waveforms (i.e., containing real P- and S-wave onsets) to the similarity of the trace to a set of ‘negative’ reference waveforms (i.e., containing P-wave coda or a flat horizontal line). A phase arrival is chosen as the center position of the window that maximizes this score function. The method has been used on various local earthquakes datasets and we test it here for the microseism dataset of the 2019 FORGE stimulation (blue square in Fig. 1). We note here that, in its current implementation stage, the algorithm is not suitable for application to continuous data for simultaneous event detection and phase picking.

3.4.1. Application to the FORGE 2019 stimulation dataset

Our set of reference waveforms includes 10 positive traces with good P- and S-wave manual picks, whereas the negative traces consist of a horizontal line. Similarly to what we observed when testing the ML models on small scale microseismic events (section 3.3), as a pre-processing step, we also had to re-scale the data by modifying the sampling rate of the seismic meta-data to enlarge the scale of the microseismicity to a similar scale of local or regional earthquakes. Traces were then bandpass filtered between 1 and 20 Hz with a Butterworth filter. In Figure 9a are shown examples of P- and S-wave auto-pick results for two events of $M_L -0.7$ (same event of Fig. 8) and $M_L -1.5$, respectively. To assess the quality of the P- and S-wave picks made by *kpick*, we used the slope of the L1-norm fit to the measurements in the Wadati diagram (Figure 9b). Any point outside the lines with slope ± 0.2 away from that of the L1-norm fit is considered erroneous and removed. Overall, *kpick* P and S-picks are in good agreement with hand-picked arrivals, and it succeeded in picking 79.2% of the total events of the initial catalog (336/424). In the majority of the cases, failure is associated with the smallest magnitudes where the SNR is very high.

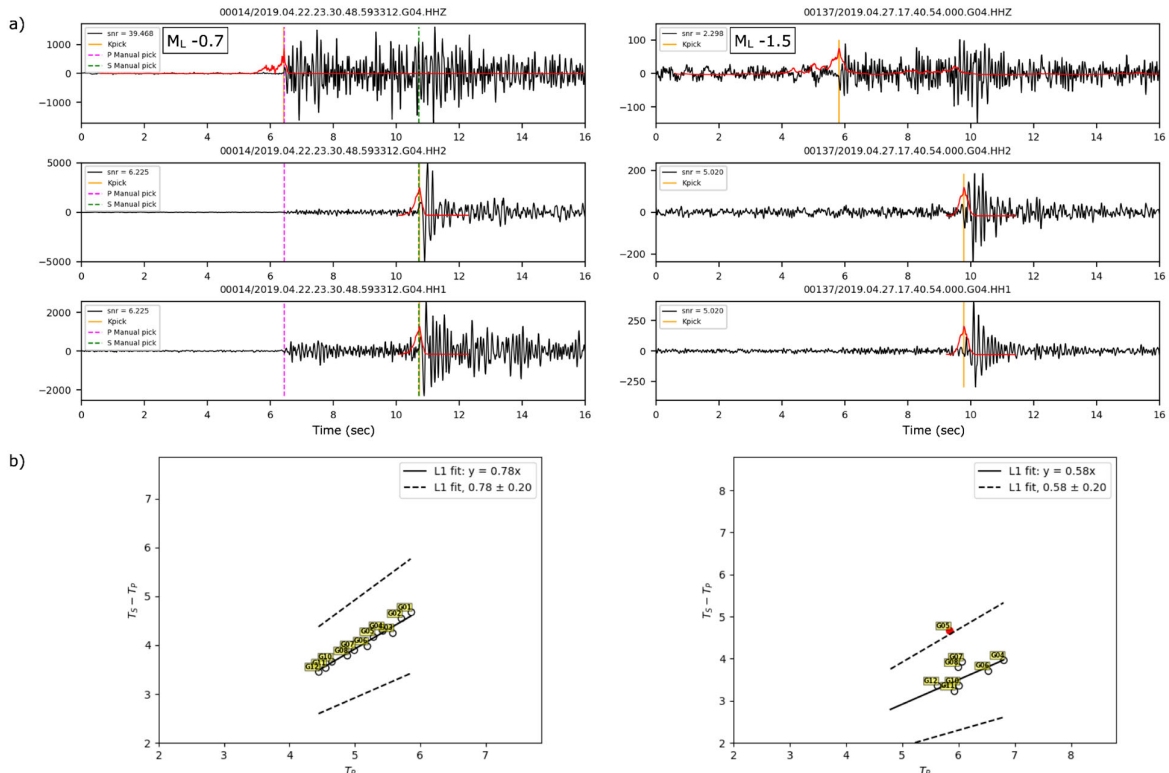


Figure 9. Results of P- and S-wave *kpick* auto-picking for two events of $M_L -0.7$ (left) and $M_L -1.5$ (right). a) Comparison of manual, and *kpick* P- and S-wave arrivals for geophone Go4. b) Wadati plot: white circles indicate the P-wave picks versus the difference between P-wave and S-wave auto-picks on all geophone stations. Red circles represent discarded picks.

4. Location of single and clustered microseismic events

We now present the new and/or adapted location algorithms that are being developed within the project in order to tackle events with short inter-event times, low magnitude or recorded by noisy DAS data.

4.1. Relative Cluster Location algorithm for DAS data

In the case of DAS data, the one-component nature of a vertically deployed DAS cable can lead to difficulties when locating seismicity. When only one single cable is present, the depth and distance from the cable may be computed using e.g., simple distance estimations from the lag-time between the P- and S-phase arrival as well as the angles of arrival. However, there is no information on the azimuth of the seismic event when the cable presents a linear geometry, unless prior information is provided. To overcome some of these challenges, we adapted the relative inter-event distance location algorithm HADES (earthquake locAtion via Distance gEometry Solvers; Grigoliet al., 2021;

<https://github.com/wulwife/HADES>) to include DAS data. In the original method, the relative distance between earthquakes is computed from the S- and P-wave arrival time differences, leading to event locations in a relative frame. Thus, the method is suitable for clustered (micro-)seismicity with sparse data coverage, and it requires only the station coordinates, a minimum of four master events with a priori known location, a homogeneous velocity model, and of course P- and S-phase picks of the events in the cluster. The uncertainty in the master events is reflected in the uncertainty of the final location of the earthquake cluster. The HADES workflow is graphically represented in Figure 10.

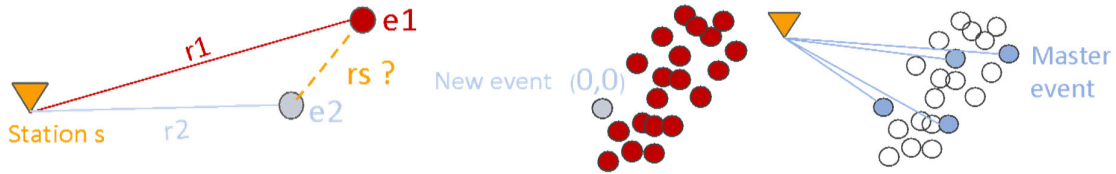


Figure 10. (Left) The inter-event distance r^s can be estimated by taking the S- and P-wave travel time (t_s and t_p , respectively) differences of two events and use the P- and S-wave velocities (v_p and v_s) to calculate the distances as $\|\mathbf{r}_{e1e2}^s\| = \mathbf{k}_v |(\mathbf{t}_s^{e1} - \mathbf{t}_p^{e1}) - (\mathbf{t}_s^{e2} - \mathbf{t}_p^{e2})|$, with $\mathbf{k}_v = \frac{v_p v_s}{(v_p - v_s)}$. (middle) This is then repeated for all inter-event distances in the cluster and then (right) the cluster can be located in an absolute frame using the master events.

Among the improvements to the original method, we now (1) require only one a-priori well-located master-event, and (2) are able to handle large arrays, such as DAS, by either considering multiple random combinations of channels or using a neural network to incorporate all channels at once. The latter is especially indicated when the position of the DAS cable with respect to the events is very ill-posed. In the original version of HADES, a coordinate system was constructed from the four master events to provide a framework for absolutely locating the rest of the events in space. With the new single master-event method, the master event is chosen as the start of the coordinate system, and four other events are located relative to this single event to construct a relative coordinate system as shown in Figure 11.

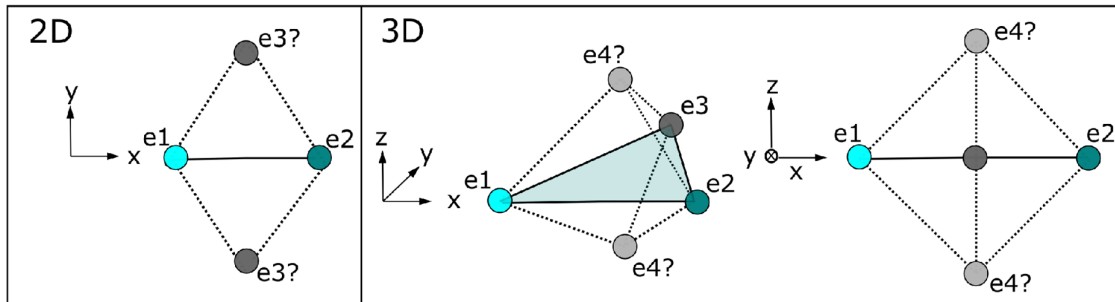


Figure 11. Construction of a relative coordinate frame to locate the events using only one master event. The left panel shows the 2D case: the master event is shown in cyan (e_1) and another event in the event cloud is located with respect to this first event (e_2). Then, by calculating the distances to e_1 and e_2 , a third event is added to the system forming a plane (e_3). Note that its azimuth with respect to the first plane will remain ambiguous. The left panel shows the 3D case: the fourth reference event (e_4) will have an ambiguous location with respect to the first plane. Thus, we can say that these 4 events form an arbitrarily oriented coordinate system that can be used to locate in a relative sense the remaining events in the seismic cluster.

The correct rotation of the cluster is found by using quaternions (see also D2.3). Quaternions are a three-dimensional version of rotations described by complex numbers, where only three complex numbers are needed to describe the total rotation. If a complex number can describe rotation about one axis: $z = a + bi$, quaternions represent rotations in 3D about an arbitrary axis with the axis components i, j, k :

$$a + bi + cj + dk,$$

which can be written as a quaternion q rotation θ about unit axis vector $v = (v_1 \ v_2 \ v_3)$:

$$q = [\cos\left(\frac{\theta}{2}\right), v_1 \sin\left(\frac{\theta}{2}\right), v_2 \sin\left(\frac{\theta}{2}\right), v_3 \sin\left(\frac{\theta}{2}\right)].$$

Here we use three quaternion rotations about three axes: (1) the vertical Z axis to rotate the seismic cluster in the latitude-longitude direction, (2) an arbitrary axis that spans the horizontal projection between a seismic station at which P- or S-wave arrivals were recorded, and the cluster barycenter, and (3) an axis orthogonal to the first two axes. In this coordinate frame the seismic cluster is then rotated until the sequence of measured arrival times at the stations are consistent with the positions of the seismic events in the cluster.

4.1.1. Application to the FORGE 2019 stimulation dataset (natural seismicity)

We applied the modified HADES to both synthetic and real data collected during the 2019 pilot stimulation at the FORGE EGS site. For the synthetic tests we considered the more favorable network configuration set up of the April 2022 configuration in order to better evaluate the resolution of the method. Figure 12 shows how the best event locations (orange dots) locate within 100 m with respect to the ground-truth input events. This shows that with multiple wells with an optimal configuration and only one master event the method can well locate the clustered seismicity and its evolution. We then apply the method to the real data recorded during 2019 stimulation at ~3 km distance from the stimulation patch (green square in Fig. 1). These are natural events of larger magnitude than the microseismicity produced by the pilot injection and thus resulting in a better signal-to-noise ratio in the DAS data. In 2019 only one DAS fiber was installed in well 78-32. As a master event we chose one well-recorded event previously located by Lellouch et al. (2021). In their work a few events were located using the surface network, but locations obtained with only the DAS remained fairly uncertain and without a robust azimuthal constraint. Although our results show that some azimuthal ambiguity remains around the cluster rotation (Figure 13), we are able to reduce the overall uncertainty by adding azimuthal and depth constraints from our method. Future improvements include using the neural-network version of HADES with additional re-trained data in order to better estimate the inter-event distance in this relatively ill-posed angular source-receiver configuration. In summary, the new version of HADES now has capabilities to locate clustered events using only P- and S- wave arrival times, one a-priori located event and large arrays (large number of channels in the case of DAS). Thus, the method is able to overcome the azimuthal uncertainty inherent to the straight-cable geometry and downhole-deployment of DAS. We demonstrated that even with only one DAS cable, and thus very unfavorable azimuthal conditions, we are able to reconstruct the shape and relative location of a seismicity cluster as a whole with reasonably low uncertainties. For individual event locations of seismic events within the cluster, the method might be less trustworthy as a final locator, but may be used as a prior for other methods to further constrain the location of the events.

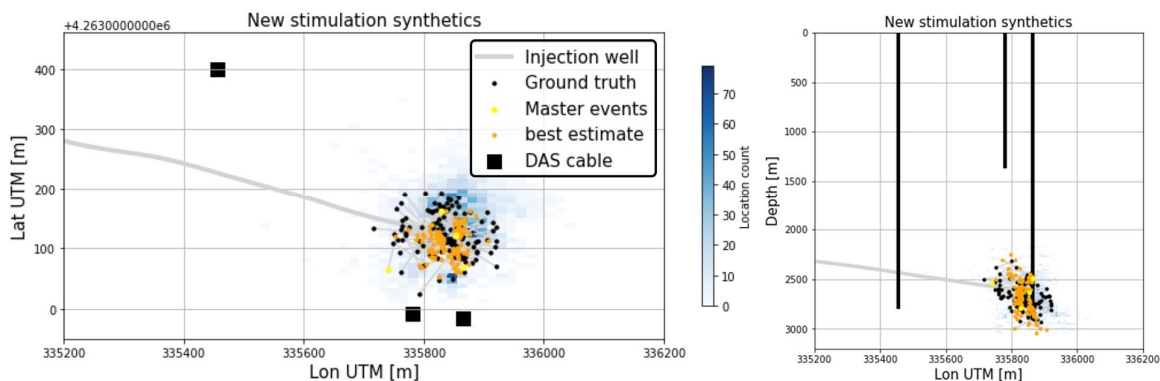


Figure 12. HADES locations for a synthetic test based on the FORGE 2022 network configuration. (Left): Map view and (right) cross section. The blue 'location count' is the number of times HADES finds earthquake locations in a specific coordinate in 150 iterations. The black dots represent the ground-truth input cluster, and the best estimate location produced by HADES is plotted with orange dots. In yellow we show the four master events used for the location, of which one is the single a-priori located master event and the other four are used to construct a relative coordinate system.

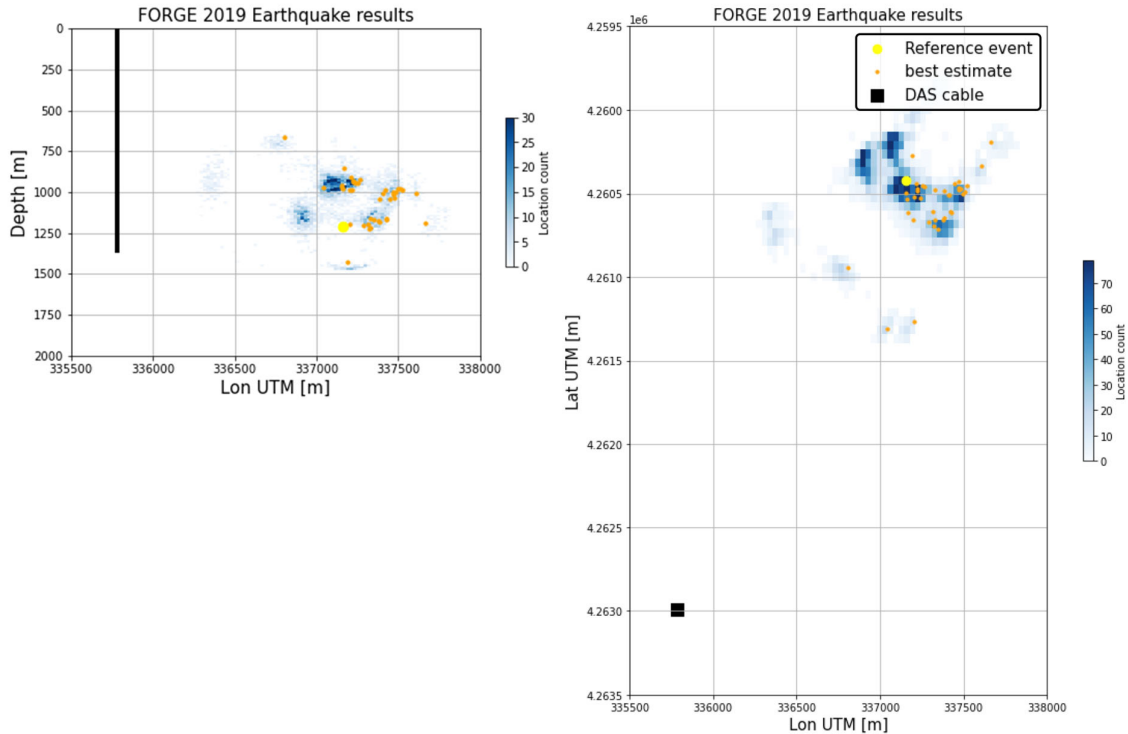


Figure 13. HADES locations for real data (natural seismicity) recorded on the DAS ~ 3 km east of well 78-32 during the 2019 stimulation. (Left) Map view, and (right) cross section. The blue 'location count' is the number of times HADES finds earthquake locations in a specific coordinate in 150 iterations. The orange dots represent the best-estimate locations produced by HADES, and the yellow dot shows the reference or master event for locating the cluster in an absolute frame.

4.2. Backprojection of phase probabilities

The migration location module of the MALMI workflow (see Deliverable 2.1, Shi et al., 2022) backprojects and stacks generated phase probabilities (for example see section 3.3) from ML-based methods in space and time for imaging seismic sources. In classical ML phase picking algorithms, a threshold is used to pick the arrival times of events, and the phase probabilities are trained to peak at the arrival time, but beyond that the phase probabilities are not used. In contrast, in the phase probability prediction module of MALMI, an adopted ML model (e.g., EQTransformer, PhaseNet) is simply used to generate continuous phase probabilities, with no explicit event detection nor phase picking, and therefore no threshold is required. The generated continuous phase probabilities are then used to associate the coherent signals and detect events across the array (for more details see Shi et al., 2022). Because no explicit phase picking or association is required, this approach can, in principle, tackle seismic events with short interevent times. With these features, the method allows us to obtain earthquake catalogs with increased detection sensitivity and improved event completeness.

The MALMI workflow requires seismic recordings from an array of stations (at least three stations in the array). Because pre-trained ML models are used to process raw seismic data and convert data to bounded values between 0 and 1, data from different types of instruments, such as broadband and short-period seismometers, strong-motion seismometers, and geophones, can be simultaneously utilized in this workflow. The location accuracy of MALMI depends mainly on the accuracy of the adopted velocity model and the ML picking uncertainties. As with other earthquake location methods, the velocity model errors and picking uncertainties will accumulate in the final location results. Because MALMI uses an Eikonal solver to build travel time tables from the input velocity models as with other travel time-based location methods (e.g., NonLinLoc), the location sensitivity to the velocity model would be the same as in these traditional methods. Since MALMI uses an array-based method (i.e., waveform migration) to locate seismic events, the geometry of the monitoring array mainly controls the location uncertainties. For example, if the monitoring array only contains surface stations, location uncertainties in depth will be larger than that in the horizontal direction.

In terms of computational costs, as MALMI needs to back-project the continuous probabilities into a 4D imaging grid (which usually have millions of grid points), MALMI is much more computationally intensive than traditional travel time-based location methods, especially for processing large nodal arrays that contain hundreds of stations. The computational cost of MALMI is mainly controlled by the total number of imaging grid points and secondly by the total number of stations in the monitoring arrays. In addition, a dense monitoring array and large monitoring area will require large computer memory as MALMI needs to build a travel time table covering all imaging grids for each station in the array. On the other hand, the ML prediction process and the waveform migration process in MALMI can be embarrassingly parallel, giving MALMI the feasibility for near real-time monitoring. For small monitoring areas with less than a hundred stations, MALMI can be deployed on a single workstation or laptop; whereas for large monitoring areas (such as ~100s km) or dense nodal arrays, MALMI should be run on an HPC.

The MALMI workflow is designed to process raw continuous seismic data and to output a seismic catalog without human intervention once the system parameters are established. The system parameters of MALMI are (1) the probability threshold, (2) the triggering number of stations and phases, (3) the coherency threshold of the stacked data volume, and (4) the variance threshold of the stacked data volume. We suggest tuning these parameters on a small sub-dataset and determining the optimal parameters before running MALMI on continuous data.

4.2.1. Application to the COSEISMIQ, Iceland, dataset

To assess the seismic monitoring performance, we compared the full MALMI workflow (all modules) with a widely used seismic monitoring software – SeisComP on one month of continuous dataset collected by the COSEISMIQ array in the Hengill geothermal area, Iceland (Grigoli et al., 2022). In total, MALMI detects and locates 694 events which are approximately 1.3 times as many seismic events as reported by SeisComP (524 events) in the same region and time range (Figure 14). Detailed catalog comparison shows that MALMI can detect and locate around 85% (444 events) of the events in the SeisComP catalog (Figure 14). As expected, these matched events detected and located by both the MALMI and the SeisComP workflow mostly consist of the high-quality events with high signal-to-noise ratios (SNR). Moreover, 250 new events are additionally identified and located, which account for 36% of events in the MALMI catalog (Figure 14). Detailed visual inspection of the waveform plots and migration profiles of many of the new events confirms that most of these new events are real and low-magnitude events and are only visible at a few stations. We also note that MALMI detects a new event of M_L 0.3 that is clearly visible at around 17 stations. Although showing high SNR and being clearly visible at many stations, this event occurs only 15 seconds after a stronger event (M_L 0.4) with a similar location. The short interevent time and significant amplitude difference likely prevented this event from being detected by the SeisComP system.

MALMI missed 15.3% of events (80) presented in the SeisComP catalog. We visually checked the undetected events and identified several reasons MALMI fails to detect these events. First, we found that some of the undetected events are, in fact, not local, but regional events. In this situation, the P and S phases of remote seismic events occurring outside the monitoring region are misidentified as two independent events by the SeisComP system and are located inside the array. Second, we noticed that a small number of events have different event locations and origin times determined by MALMI and SeisComP, thus they do not match when comparing the two catalogs (matched events should have an origin time difference within 1 s and location difference within 5 km). Third, we found that some events are indeed detected by MALMI, but are subsequently removed after the migration process, because they do not pass the energy focus criterion. This criterion is set in place to assess whether the backprojected energy converges; convergent source energy after backprojection and stacking will have stacked energy larger than 0.075 ($C_{max} \geq 0.075$) and a standard deviation of the migrated volume smaller than 0.145 ($std(C) \leq 0.145$). This indicates that, compared to simple threshold criteria, a more dedicated tool for assessing the energy focusing might improve MALMI's performance. Finally, because a pre-trained ML model on global labeled data is used in the MALMI workflow, we observe that some region-specific signals are sometimes missed by the ML models, thus preventing the identification of locatable seismic events, even though a very low threshold is employed during the detection process.

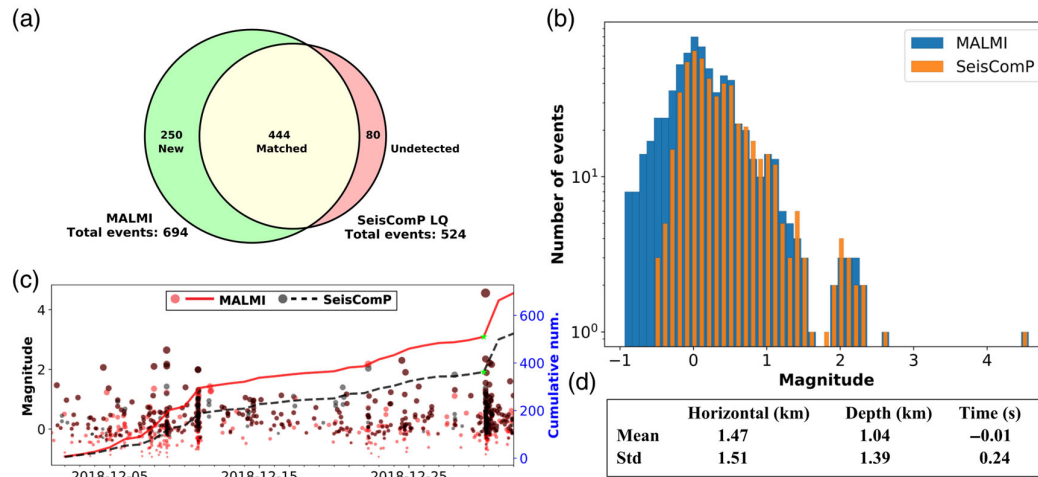


Figure 14. Comparison between the MALMI catalog and the SeisComp catalog. (a) Venn diagram showing the detection capability statistics for the two catalogs. (b) Non-cumulative frequency-magnitude distribution of earthquakes in the MALMI and SeisComp catalogs. (c) Earthquake magnitude versus time. The red dots denote events in the MALMI catalog, whereas the black dots represent events in the SeisComp catalog. Event size is scaled by magnitude. The red solid line and black dashed line show the cumulative number of events (right Y-axis) over time for the MALMI and SeisComp catalogs, respectively. The green star denotes the occurrence of the largest event (M_L 4.5 event at UTC: 30 December 2018 T02:56:20) in the monitoring time period. (d) The mean and standard deviation of the location (in both horizontal and depth directions) and origin time differences for the codetected events in the two catalogs.

4.3. Earthquake locations from elastic Time-Reverse Imaging (TRI)

Time Reverse Imaging (TRI) refers to a waveform-based migration location scheme. The same mathematical principles of station-receiver reciprocity of the wave equation and reciprocity in time is used as for the backprojection location method reported in section 4.2. However, instead of calculating tables, we used an elastic waveform simulator. The basic principle is to back propagate continuous raw waveforms using a numerical solver for the seismic wave propagation and an adequate velocity model. The wavefield will then converge at the original source location. In media without damping and if the complete wavefield is recorded (i.e. an infinite number of sensors), the back propagated wavefield will converge at the true source location without any uncertainty. In real world applications, the location accuracy strongly depends on the sensor distribution and the quality of the velocity model. For surface station networks, the inter-station distance and maximum aperture of the network define the subsurface volume in which sources can be located (Werner & Saenger, 2018). The resolution of the velocity model needs to fit the frequency of waveform signals used in the back propagation. In principle, the TRI workflow can be automatized. To this end, a model can be initialized at the beginning that is fed with continuous raw waveforms to produce source images in regular time steps. Then, a ML method trained for identification of sources from the source images can be used to produce a catalog. However, near real time application is hindered by the fact that a numerical simulator is used for propagation of the full seismic wavefield. For three-dimensional applications with sufficient spatial resolution, a high-performance cluster computer needs to be used. Even using very large cluster computers, the state-of-the-art numerical simulators cannot provide near real-time simulations. There are approaches to use GPU computations which decrease computation times by about 18 times (Xue et al., 2015). For simulations that take 6 hours on a CPU cluster, this means a computation time of about 20 minutes. This is far from real time applications and can only be slightly improved on by innovative numerical simulators. Therefore, we see the benefit of using a backprojection migration method (as reported in section 4.2) in combination with a posterior analysis of questionable waveform sections using elastic TRI. The overwhelming benefit of combining real-time waveform-based methods with elastic TRI on targeted time windows is that the resolution of the source, especially of low-phase probability events or events with small inter-event time, is effectively enhanced. This opens the possibility for a near-real time production of a catalog of high-resolution source images.

4.3.1. Application to Los Humeros, Mexico, dataset

The TRI workflow is applied to a dataset recorded at the geothermal site Los Humeros in Mexico (Finger & Saenger, 2021). The surface network included 10 short-period and 17 broadband stations. At the time of the study, only a one-dimensional velocity model was available. For demonstration purposes and to test the methodology, TRI was applied to sections of the continuous waveform where local earthquakes were already detected. Two time segments are used here: The first one starts at 22 April 2018 21:03:45 and the second one starts at 29 April 2018 22:49:50. After removing artificial convergences (false positives) from the dataset, we found three detections for the time segment used on 22 April 2018 (Figure 15), whereas two detections were identified for the time segment from 29 April 2018 (Figure 16). For each time segment, the catalog only reported one event each. This shows how TRI was able to increase the detection sensitivity. From observations of the waveforms, it becomes clear that these additional events have very small inter-event times and the smaller magnitude events are thus masked by the earlier larger events.

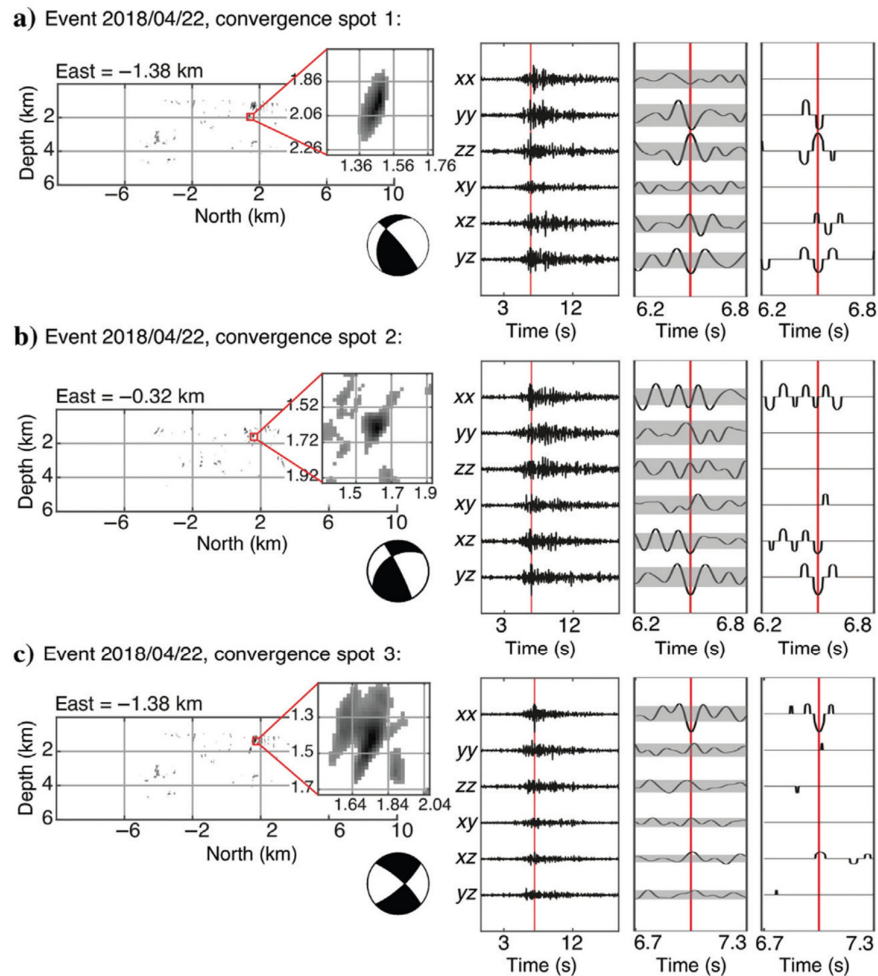


Figure 15. Location and characterization result for the events after 22 April 2018 21:03:45

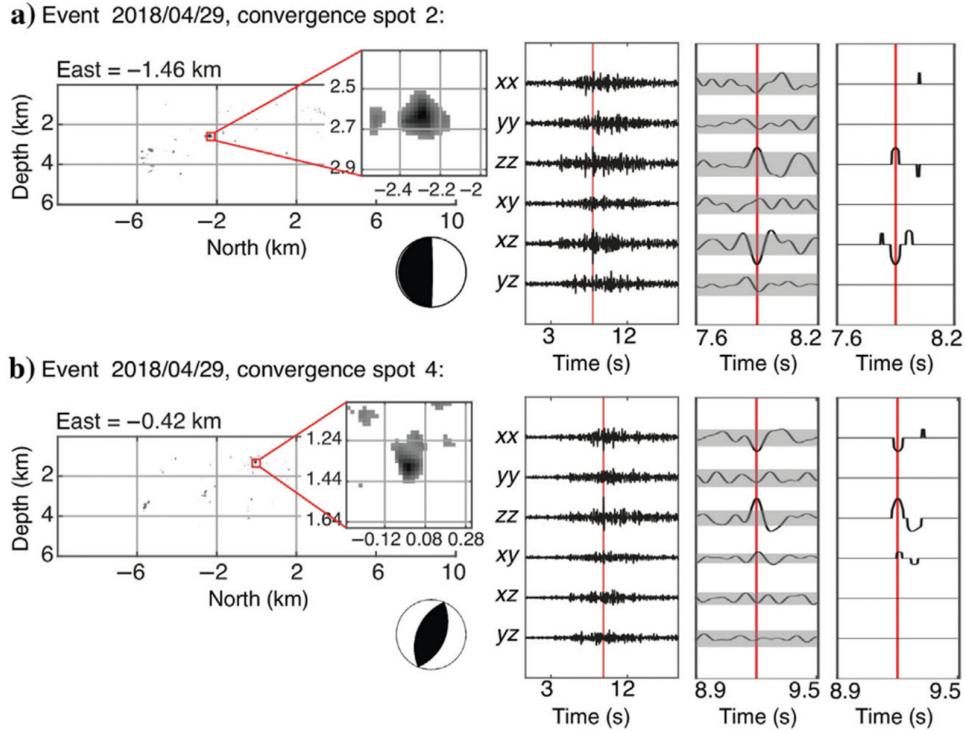


Figure 16. Location and characterization results for the event on 29 April 2018 after 22:49:50.

4.3.2. Application to preliminary synthetic dataset at the FORGE EGS site

The TRI workflow is applied to synthetic data generated for the FORGE EGS site. The initial set up consists of regular distributed sources and the velocity model derived from Zhang & Pankow (2021) and Lellouch et al. (2020). Two tests were carried out: (1) using only a network configuration of very dense surface stations (Figure 17a), and (2) using an additional two vertical lines of receivers that mimic borehole sensors (Figure 17b). Using only the surface stations, the vertical uncertainty is much higher than the horizontal uncertainty, as expected. When the additional well sensors are used, the augmented azimuthal coverage improves the overall accuracy. Especially for the sources in between the well sensors, the accuracy improves significantly. This preliminary test shows that with the sensor setup at FORGE both during the 2019 pilot stimulation and the 2022 stimulation, elastic TRI is able to produce locations with high accuracy. Very similar accuracies are expected for the method described in section 4.2, albeit the overall resolution might be reduced due to limits of the memory space for the travel-time tables and thus reduction of grid points.

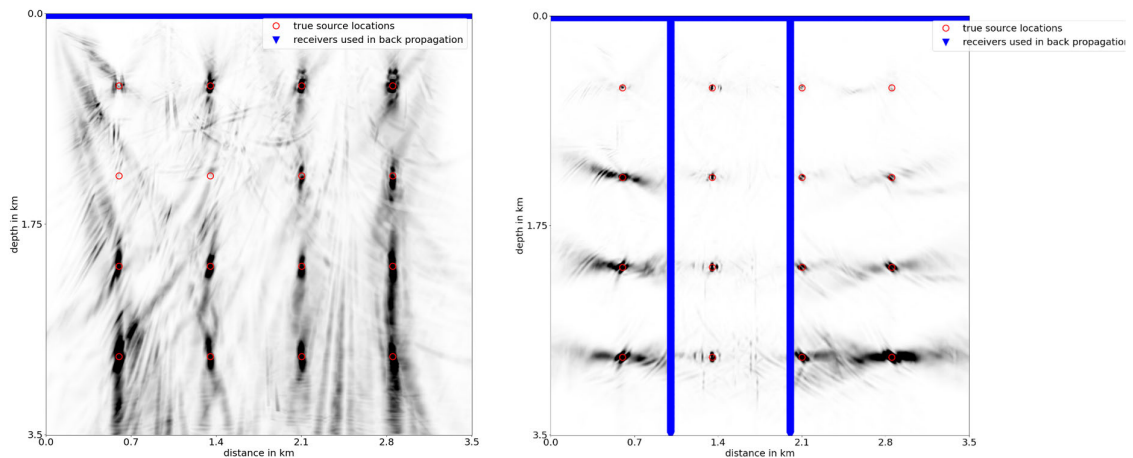


Figure 17. TRI results using very dense surface stations (left) and very dense surface stations plus two lines of vertical borehole sensors (right). For the borehole stations, only the z component of the displacement is used. Total energy density is shown as a gray scale. Data is cleaned using illumination map following Finger and Saenger (2020).

5. Conclusions and Outlook

In the current deliverable we have shown methods for detection and location of (micro-) seismic events. Results from different datasets highlight the vast capabilities of these innovative methods. In the context of geothermal projects with thousands of micro-seismic events, short inter-event times, low magnitudes and often unfavorable azimuthal coverage, the methods presented here are clearly superior to conventional methods. Results show a general decrease in location uncertainty and in magnitude of completeness. However, we also show that the application in near real-time to a variety of case sites remains challenging.

A qualitative comparison of all methods presented in this deliverable is summarized in Table 1. First, the individual needs of the methods are outlined, followed by a qualitative assessment of accuracy, real-time capability and automatization of each method.

Table 1: Qualitative comparison of the described methods. *R = requires; C = can use; X = cannot use

	Semblance based DAS picker (section 3.1)	ML-based picker (section 3.2)	Conventional pickers (section 3.4)	HADES with DAS (section 4.1)	MALMI (section 4.2)	TRI (section 4.3)
HPC/Parallelization	C (currently not implemented)	C	X	X	R	R
3D velocity model	<i>not relevant</i>	<i>not relevant</i>	<i>not relevant</i>	X	C (currently not implemented)	C
Large number of stations	<i>not relevant</i>	C	C	X (C with neural networks)	C	R
Benefits from GPU acceleration	C (currently not implemented)	C	X	X	C (currently not implemented)	C
Surface or borehole stations	X	C	R	C	C	C
DAS data	R	C	X	R	C (currently not implemented)	C
Qualitative ranking						
Spatial uncertainty	<i>not applicable</i>	<i>not applicable</i>	<i>not applicable</i>	medium	high	high
Temporal precision	high	high	medium	<i>not applicable</i>	high	high
(potential for) real-time application	high	high	variable (*low for <i>kpick</i> , but high for STA/LTA)	low	medium-high	low
(potential for) automatization	high	high	variable	medium	high	medium

In this short report we have demonstrated that ML-based pickers are generally superior to conventional pickers. On the other hand, ML-based detectors need to be adjusted for the seismicity of each site and a training step might be necessary for each site to ensure the highest quality of detections. The new detection method for DAS presented here highlighted

how events detection in DAS is still challenging given the high-level of noise and unknown coupling of the cables. There are currently no standard installation recommendations and thus each DAS system has a different seismic response.

In terms of location methods, waveform-based methods such as those presented here (MALMI and TRI) are able to produce very high accuracy locations down to one wavelength of used frequency content. The very high computational efforts of TRI are reduced by using pre-calculated traveltimes tables such as is done in MALMI. However, near real time analysis is still computationally expensive in 3D media and requires additional computational resources such as high-performance clusters or parallelization. Using relative locations of clustered seismicity (HADES) provides a significant jump in computational efficiency and is especially valuable in geothermal applications where events often occur in clusters. The integration with DAS data is promising due to its high spatial sampling and short distance to the event cluster. However, DAS data is typically very large and takes a long time to transfer from the acquisition computer to the computer running the analysis, prohibiting near real time application for the time being.

Thus, an integrated approach of the presented methods might be the key for balancing accuracy and near real time results. For example, ML-based pickers can aid in selecting appropriate time windows for backprojection and time-reverse imaging (as demonstrated in MALMI), thus reducing the computational cost, and increasing the potential for real-time monitoring. In terms of accuracy, locations from waveform-based methods could help orient the clustered seismicity in HADES in the absolute spatial domain, thus also providing an increase location resolution when the azimuthal coverage is insufficient. This is often the case in EGS projects when often only one monitoring well is available for monitoring the seismicity.

In the remainder of the project time, we plan to make step changes in tackling some of these goals by further developing and comparing the presented methods on two common datasets: the synthetic test bench currently under development and the data of the April 2022 stimulation at FORGE. While the first allows us to compare true errors and identify and overcome problems of each method, the second demonstrates the applicability to real data of a geothermal reservoir. The standardized approach using the synthetic testbench will be available in the future as an open-source toolbox (Task 5.3). The goal is to build a flexible wrapper in the form of a Jupyter Notebook where predefined structural elements, velocity models, sources and receivers can be added and removed in a convenient manner, and can be run on remote sites for models on several scales. Simulations from a variety of models can then be compared to recorded microearthquakes in order to assess their benefit for the model-data misfit. This will also allow to establish a benchmark metrics to assess how 'good' a model is, and how it compares to others. This will provide a rational baseline for testing network performances and develop good practice guidelines (Task 5.1).

We will work on defining a workflow to optimally detect and locate microseismic events in near real time within the technology limitations. Ideally, this may be integrated into a larger modeling workflow. For example, forecasted seismicity models could be integrated with the wave propagation solver in order to forecast ground motion. The overarching goal is to implement this workflow at the next stimulation in FORGE in real time (M2.5, M4.5).

Liability Claim

Reference List

- Finger, C. & Saenger, E.H. (2021). Determination of the time-dependent moment tensor using time reverse imaging. *Geophysics*, 86 (2), KS63–KS77.
- Finger, C. & Saenger, E. H. (2020). Sensitivity Maps for Time-Reverse Imaging: An Accuracy Study for the Los Humeros Geothermal Field (Mexico). *Geophysical Journal International*, 222, 231–246.
- Gaucher, E., Toledo, T., Metz, M., Figueroa-Soto, A. G., & Calò, M. (2019). One year of passive seismic monitoring of the Los Humeros (Mexico) geothermal field. European Geothermal Congress 2019. Den Haag, The Netherlands, 11-14 June 2019.
- Grigoli, F., Clinton, J.F., Diehl, T. *et al.* (2022). Monitoring microseismicity of the Hengill Geothermal Field in Iceland. *Scientific Data* 9, 220. <https://doi.org/10.1038/s41597-022-01339-w>.
- Grigoli, F., Ellsworth, W. L., Zhang, M., Mousavi, M., Cesca, S., Satriano, C., Beroza, G. C., & Wiemer, S. (2021). Relative earthquake location procedure for clustered seismicity with a single station. *Geophysical Journal International*, 225(1), 608–626.
- Lellouch, A., Lindsey, N. J., Ellsworth, W. L., & Biondi, B. L. (2020). Comparison between Distributed Acoustic Sensing and Geophones: Downhole Microseismic Monitoring of the FORGE Geothermal Experiment, *Seismol. Res. Lett.* 91, 3256–3268.
- Lellouch, A., Schultz, R., Lindsey, N. J., Biondi, B. L., & Ellsworth, W. L. (2021). Low-magnitude seismicity with a downhole distributed acoustic sensing array—Examples from the FORGE geothermal experiment. *Journal of Geophysical Research: Solid Earth*, 126(1), e2020JB020462.
- Li, L., Tan, J., Schwarz, B., Staněk, F., Poiata, N., Shi, P., Diekmann, L., Eisner, L., & Gajewski, D. (2020). Recent advances and challenges of waveform-based seismic location methods at multiple scales. *Reviews of Geophysics*, 58, e2019RG000667. <https://doi.org/10.1029/2019RG000667>.
- Löer, K., Toledo, T., Norini, G., Zhang, X., Curtis, A., & Saenger, E. H. (2020). Imaging the deep structures of the Los Humeros geothermal field, Mexico, using three-component ambient noise beamforming. *Seismological Research Letters*, 91 (6): 3269–3277.
- Moore, J., McLennan, J., Pankow, K., Simmons, S. Podgorney, R., Wannamaker, P., Jones, C., Rickard, W., & Xing, P. (2020). The Utah Frontier Observatory for Research in Geothermal Energy (FORGE): A Laboratory for characterizing, creating and sustaining Enhanced Geothermal Systems, Proc. of 45th Workshop on Geothermal Reservoir Engineering Stanford University, 1–10.
- Mousavi, S. M., Ellsworth, W. L., Zhu, W., Chuang, L. Y., & Beroza, G. C. (2020). Earthquake transformer—an attentive deep-learning model for simultaneous earthquake detection and phase picking. *Nature communications*, 11(1), 1–12.
- Neidell, N. S., & Taner, M. T. (1971). Semblance and other coherency measures for multichannel data. *Geophysics*, 36 (3): 482–497. doi: <https://doi.org/10.1190/1.1440186>.
- Pankow, K., Mesimeri, M., Mclennan, J., Wannamaker, P., & Moore, J. (2020). Seismic monitoring at the Utah frontier observatory for research in geothermal energy, Proc. of 45th Workshop on Geothermal Reservoir Engineering Stanford University, 1–9.
- Quinteros, J., Carter, J. A., Schaeffer, J., Trabant, C., Pedersen, H. A. (2021). Exploring Approaches for Large Data in Seismology: User and Data Repository Perspectives. *Seismological Research Letters*, 92 (3): 1531–1540. doi: <https://doi.org/10.1785/0220200390>
- Rawles, C., & Thurber, C. (2015). A non-parametric method for automatic determination of *P*-wave and *S*-wave arrival times: application to local micro earthquakes, *Geophysical Journal International*, 202 (2), 1164–1179, <https://doi.org/10.1093/gji/ggv218>.

- Ross, Z. E., Meier, M. A., Hauksson, E., & Heaton, T. H. (2018). Generalized Seismic Phase Detection with Deep Learning Short Note. *Bulletin of the Seismological Society of America*, 108(5A), 2894-2901.
- Shi, P., Grigoli, F., Lanza, F., Beroza, G. C., Scarabello, L., & Wiemer, S. (2022). MALMI: An Automated Earthquake Detection and Location Workflow Based on Machine Learning and Waveform Migration. *Seismological Research Letters*; doi: <https://doi.org/10.1785/0220220071>.
- Toledo, T., Gaucher, E., Malte, M., Calò, M., Figueroa, A., Jousset, P., Kieling, K., & Saenger, E. (2019). Dataset of the 6G seismic network at Los Humeros, 2017-2018. GFZ Data Serv.
- Xue, Q., Wang, Y., Zhan, Y., & Chang, X. (2015). An efficient GPU implementation for locating micro-seismic sources using 3D elastic wave time-reversal imaging. *Comput. Geosci.*, 82:89{97}.
- Zhang, H., & Pankow, K. L. (2021). High-resolution Bayesian spatial autocorrelation (SPAC) quasi-3-D Vs model of Utah FORGE site with a dense geophone array. *Geophysical Journal International*, 225(3), 1605-1615.
- Zhu, W., & Beroza, G. C. (2019). PhaseNet: a deep-neural-network-based seismic arrival-time picking method. *Geophysical Journal International*, 216(1), 261-273.
- Wannamaker, P., Simmons, S., Miller, J., Hardwick, C., Erickson, B., Bowman, S., Kirby, S., Feigl, K. & Moore, J. (2020). Geophysical Activities over the Utah FORGE Site at the Outset of Project Phase 3, Proc. of 45th Workshop on Geothermal Reservoir Engineering Stanford University, 1–14.
- Werner, C. & Saenger, E. H. (2018). Obtaining reliable source locations with time reverse imaging: Limits to array design, velocity models and signal-to-noise ratios. *Solid Earth*, 9(6):1487{1505}.
- Woollam, J., Münchmeyer, J., Tilmann, F., et al. (2022). SeisBench—A toolbox for machine learning in seismology. *Seismological Society of America*, 93(3), 1695-1709.